



# Superachromatic polarization modulator for stable and complete polarization measurement over an ultra-wide spectral range

HONGGANG GU,<sup>1</sup> HAO JIANG,<sup>1,2</sup> XIUGUO CHEN,<sup>1</sup> CHUANWEI ZHANG,<sup>1</sup> AND SHIYUAN LIU<sup>1,3</sup>

<sup>1</sup>State Key Laboratory of Digital Manufacturing Equipment and Technology, Huazhong University of Science and Technology, Wuhan, Hubei 430074, China

<sup>2</sup>hjiang@hust.edu.cn

<sup>3</sup>shyliu@hust.edu.cn

**Abstract:** The polarization measurement system deals with polarized light-matter interactions, and has been a kind of powerful optical metrology applied in wide fields of physics and material. In this paper, we address several general theoretical aspects related to the system model and optimization for linear polarization systems from a view of the matrix algebra. Based on these theories, we propose a new framework of superachromatic polarization modulator (PM) by combining a linear polarizer and a sequence of parallel linear retarders (LRs) for a typical kind of linear polarization system based on the rotating compensator (RC) principle. In the proposed PM, the LRs are made of quarter-wave plates and as a whole act as the RC. Compared with conventional achromatic/superachromatic composite waveplates, the LR sequence has general axis orientations and is optimized by the condition number of the instrument matrix of the PM, which thereby provide much more flexibility to achieve uniform, stable and complete polarization modulation over ultra-wide spectral range. The intrinsic mechanisms, including the working principle, optimization strategy and *in-situ* calibration method of the proposed PM, are presented and revealed mathematically by the matrix algebra. Results on several prototypes of the PM demonstrate the validity and capability of the proposed methods for applications in broadband polarization measurement systems. The fabricated PM is further applied to a home-made dual RC Mueller matrix ellipsometer, and the accuracy and precision in the full Mueller matrix measurement are better than 2‰ and 0.6‰ respectively over the ultra-wide spectral range of 200~1000 nm. Compared with existing techniques, the proposed PM has advantages due to superachromatic performances over ultra-wide spectral ranges, stable and complete modulation of the polarized light, and convenience for adjustment and calibration.

© 2022 Optica Publishing Group under the terms of the [Optica Open Access Publishing Agreement](#)

## 1. Introduction

A polarization measurement system detects and analyzes the polarized light-matter interactions by modulating and demodulating the polarization state of the light, which is a kind of powerful optical metrology with many attractive merits, such as low cost, non-destruction, and high throughput [1–8]. Polarization systems and devices, such as polarimeters and ellipsometers, have been widely applied in various fields, including the nanomaterial and nanostructure characterization [9–25], remote sensing [26–28], astronomical exploration [8,29,30], and biomedical diagnosis [31,32], etc. Since the additional polarization dimension of light is introduced, these related systems can acquire much more information than the conventional devices without polarization, which has been proved to significantly improve the key systematic performances, such as the contrast and sensitivity [17,28,32], and to provide more knowledge about the samples or objectives, such as the optical anisotropy [15–19]. Therefore, developing high-precision, broadband and

complete polarization systems has continuously been a hot research topic for more than one century [5,33–35].

The polarization modulator (PM) is the key component in a polarization system to modulate and demodulate the polarization state of the light [1–3,5]. Polarization characteristics, such as the retardance, diattenuation, rotation angle, and axis azimuth, of the PM determine the final performance of systems [36–40]. Additionally, the dispersion in these characteristics limits the applicable spectral range of the polarization system [5]. Generally speaking, any element that can change the polarization state of light can be used as the PM [41–65], such as the polarizer [41–43], retarder [44–57], anisotropic mirrors [58,59], etc. Polarization modulation can be achieved typically through mechanical rotation [41–46], electric-driving modulation [51–57], or spatial division of amplitude [66–69], etc. However, in the implementation of a polarization system, the PM design involves several practical considerations, such as the applicable spectral range, the precision and efficiency, and the completeness of polarization modulation. For example, a linear polarizer (LP) can generate, modulate, and analyze the linearly polarized light [1]. A linear retarder (LR), including the waveplate, the liquid crystal retarder, and the photoelastic modulator, can only change the polarization state of the polarized light by introducing a phase retardation between the two polarized components, but cannot generate nor analyze the polarized light [1]. Usually, the combination of a LP and a LR is used to achieve complete polarization modulation, in which, the LP is fixed to generate linear polarized light, and the LR is rotated to compensate and modulate the polarized light [1–3].

There are several configurations of complete PMs, typically including: (i) one fixed LP + one rotating LR (also called rotating compensator, RC) [44–46], (ii) one fixed LP + two liquid variable retarders [52–54], (ii) one fixed LP + two photoelastic modulators [57,68], and (iii) spatial division-of-amplitude four/six channels [66–69], and (iv) one rotating LR + one division of focal plane (DoFP) polarization camera [70,71], etc. Among these configurations, the PM based on liquid variable retarders cannot be used over the ultraviolet (UV) spectral range because the UV light may damage the liquid crystal molecules [72]. The configuration based on photoelastic modulators can achieve high-precision complete polarization modulation over an ultra-wide spectral range from the UV to near infrared region. However, for broadband applications, the voltage-driven photoelastic modulator will introduce much more complexity for the system calibration and data processing, which may severely reduce the measurement accuracy and speed [3,56,57]. The spatial division-of-amplitude multi-channel polarimetry and ellipsometry simultaneously detect multi-channel signals, which make it faster than the temporally multi-channel devices. However, in the spatial division-of-amplitude multi-channel polarimetry and ellipsometry, each channel needs individual polarized elements (including the polarizers, retarders and splitters, etc.) and specific optical path debugging and alignment, which make it complex and bloated, and limit the application [66,68]. In comparison, the LP-RC configuration is the most popular and widely used PM in polarization systems.

The most commonly used RCs include Fresnel prisms and birefringent waveplates. Although specially designed Fresnel prisms can be applied as superachromatic compensators for broadband RC-based systems [49,50,73,74], they may introduce severe diattenuation, similar to the dichroism, especially over the UV range, leading to considerable complexity to the calibration and additional error sources to the system [74]. The true zero-order waveplate (i.e., a single waveplate) and biplate (also referred to as the compound zero-order waveplate) as well as their alternatives, such as the monoplate and Berek plate, are the most widely applied waveplate compensators [5,7,75]. However, the strong dispersion of birefringent materials extremely limits the applicable spectral ranges of these non-achromatic waveplates. To broaden the applicable spectral range, composite waveplates consisting of multiple single waveplates are designed as achromatic or superachromatic retarders, such as Pancharatnam waveplate [76], Beckers waveplate [77], and their extensions [47,76–86]. However, these conventional designs fall in the trap to make

achromatic LRs, and the single waveplates are always arranged in a symmetric architecture or with their fast axes perpendicular/parallel to each other. For a polarization system, what we care about is the total effect of the compensator on the immunity of the system to the errors [39,87], but not whether it is a LR or not. The specific structures of conventional designs not only significantly sacrifice the optimization freedoms to adapt to the broadband polarization system, but also make them too complicate to be fabricated. Another limitation in conventional designs is that the evaluation criterion for achromatism is always the retardance, e.g., quarter-wave ( $90^\circ$ ), half-wave ( $180^\circ$ ), etc., which is not suited to directly and comprehensively evaluate the performance of the polarization system. Recently, some pioneer works have broken this rigid design framework and customized superachromatic compensators based on multiple waveplates for the broadband systems [48,87,88]. While, these published compensators were designed only for specific systems, such as the Stokes polarimeter [48], the dual rotating-compensator Mueller matrix ellipsometer (DRC-MME) [87], or the rotating-compensator imaging Stokes polarimeter [88]. The intrinsic mechanism behind them remains to be explored and generalized to easily popularize the applications to various broadband polarization systems.

In this paper, we aim to propose a general form to design stable and complete PMs for all broadband linear polarization systems based on the RC principle. Based on this consideration, we will firstly address several general theoretical aspects for linear polarization systems using the matrix algebra in Sec. 2. Based on these theories, then we propose a new framework of a superachromatic PM by combining a LP and a sequence of parallel LRs to achieve stable and complete polarization modulation over an ultra-wide spectral range in Sec. 3. The working principle, optimization strategy, and *in-situ* calibration method of the proposed PM are presented for all systems based on the RC principle. Finally, in Sec. 4, prototypes of the proposed PM are designed and manufactured, and further applied to a DRC-MME to demonstrate the effectiveness and capability of the proposed theory and method.

## 2. General theoretical aspects for linear polarization systems

### 2.1. Mathematical model for linear polarization system

In a linear polarization system, the detected intensity can be expressed as a linear function of the polarimetric parameters to be determined

$$i = a_0 + \sum_{l=1}^L a_l \zeta_l, \quad (1)$$

herein,  $\zeta_l$  ( $l = 1, 2, \dots, L$ ) represents the Stokes vector element, Mueller matrix element, or a polarimetric parameter in any other form (e.g., ellipsometric angles and their derivatives),  $L$  is the total number of polarimetric parameters to be measured,  $a_0$  and  $a_l$  are coefficients related to the configuration of the polarization system, which is determined by the properties of the polarized components, such as the axis azimuth, retardance, diattenuation, etc.

In practice, to achieve the measurement of multiple polarimetric parameters, temporally or spatially multi-channel configurations are usually constructed for the polarization system. In this case, each channel corresponds to a specific configuration, and thus can be mathematically described by a linear function in form of Eq. (1). Consequently, the system transfer function of a multi-channel linear polarization system can be written in the following matrix form

$$\mathbf{I} = \mathbf{D}(\mathbf{b}) \cdot \mathbf{S}, \quad (2)$$

where,  $\mathbf{I} = [i_1, i_2, \dots]^T$  is a  $K \times 1$  intensity flux vector with the  $k$ -th element being  $i_k$ , and  $K$  is the total number of the detected intensities,  $\mathbf{D}$  is a  $K \times L$  coefficient matrix, usually called the instrument or measurement matrix of the polarization system,  $\mathbf{b}$  represents the set of systematic

parameters of the polarization system, such as the azimuth, retardance, diattenuation, etc., and finally  $\mathbf{S}$  is an  $L \times 1$  column vector summarizing the polarimetric parameters to be measured.

Equation (2) gives a general mathematic model of a multi-channel linear polarization system, and provides an intuitive view to understand its working principle. The calibration and measurement process of the linear polarization system can be respectively described as

$$\mathbf{D}(\mathbf{b}) = \mathbf{I} \cdot \mathbf{S}^+, \quad (3)$$

$$\mathbf{S} = \mathbf{D}(\mathbf{b})^+ \cdot \mathbf{I}, \quad (4)$$

where, the superscript “+” indicates the Moore-Penrose pseudo-inverse of a matrix.

It can be seen that the instrument matrix  $\mathbf{D}(\mathbf{b})$  plays an extremely important role throughout the construction of the linear polarization system, including not only the system calibration and data processing, but also the system optimization and even error analysis and correction. Here, two indices, namely the rank and the condition number (CN) of the instrument matrix are applied to respectively evaluate the completeness and stability of the linear polarization system.

The rank of the instrument matrix is defined as

$$r(\mathbf{D}) = \text{rank}(\mathbf{D}). \quad (5)$$

When the rank of instrument matrix  $r$  just equals to the number ( $L$ ) of polarimetric parameters in  $\mathbf{S}$ , we call it a complete polarization system. If  $r$  is larger than  $L$ , the polarization system is complete and overdetermined. Otherwise, if  $r$  is less than  $L$ , the polarization system is underdetermined and incomplete. It should be noted that the number of polarimetric parameters in vector  $\mathbf{S}$  is also a basis to judge the completeness of the polarization system [89].

The CN of the instrument matrix is defined as

$$\kappa_p(\mathbf{D}) = \|\mathbf{D}\|_p \|\mathbf{D}^+\|_p, \quad (6)$$

where, the notation  $\|\cdot\|_p$  represents the  $p$ -norm of a matrix, and  $p = 1, 2, F$ , and  $\infty$  respectively represent the 1-norm, 2-norm, Frobenius-norm, and infinity norm. The CN indicates the singularity of the instrument matrix, which evaluates the stability, namely the immunity to errors, of polarization system. The CN of a unit matrix is 1, while that of a singular matrix is  $\infty$ . Therefore, the polarization system becomes stronger when the CN becomes smaller. It should be noted that other metrics, such as the equally weighted variance (EWV), matrix determinant, signal-to-noise ratio, etc., can also be utilized to evaluate the singularity of the instrument matrix [90–94]. These metrics have been proved to be equivalent to each other mathematically [95].

## 2.2. Equivalence of PSG and PSA

Polarization systems usually contain two basic modules, namely the polarization state generator (PSG) and the polarization state analyzer (PSA). Figure 1 depicts a general schematic of a sequence of basic polarized elements with a linear polarizer (LP) in the head/end. When the light propagates through the sequence from the direction with the LP in the head, it plays as a PSG in the polarization system. Otherwise, the sequence acts as a PSA when the light propagates from the opposite direction with the LP in the end. The systematic transfer matrix of the PSG and PSA can be respectively calculated by multiplying the Mueller matrices of the polarized elements in sequence from two opposite directions. Based on the optical reversibility theorems for polarization [96], we have the following equivalence for the PSG and PSA,

$$\mathbf{M}_{\text{PSG}} = \mathbf{M}_M \cdots \mathbf{M}_2 \mathbf{M}_1 \mathbf{M}_{\text{LP}}, \quad (7)$$

$$\mathbf{M}_{\text{PSA}} = \mathbf{M}_{\text{LP}}^T \mathbf{M}_1^T \mathbf{M}_2^T \cdots \mathbf{M}_M^T = \mathbf{M}_{\text{PSG}}^T, \quad (8)$$

where,  $\mathbf{M}_m$  and  $\mathbf{M}_m^T$  ( $m = 1, 2, \dots, M$ ) are the Mueller matrix and its transpose of the  $m$ -th polarized element in the sequence. The Mueller matrix of a polarized element, such as the linear retarder (LR), the LP, and the rotator can be seen in Refs. [1–3].

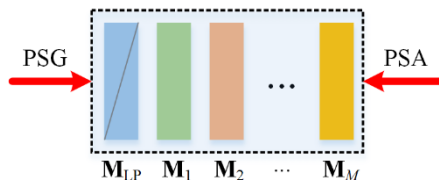


**Fig. 1.** Schematic of a general PSG/PSA containing a sequence of polarized components at least with a linear polarizer in the head/end.

Therefore, we have an important conclusion that the systematic transfer matrix of a PSG is the transpose of that of a PSA with the same configurations. They have the same characteristics, including the completeness (rank) and stability (singularity), for polarization modulation. Thus, from the point of matrix optics, we say the PSG and PSA with the same configurations are equal for the polarization modulation.

### 2.3. Optimization metric based on condition number

In practice, the polarization measurements invariably have disturbances and noises associated with the detected intensities  $\mathbf{I}$  and the instrument matrix  $\mathbf{D}$  [97]. Meanwhile, the polarization system can be operated under different configurations, which have different immunity to the errors. In the design of a polarization system, we should optimize the configurations to make the system have the strongest immunity. Since it is a common practice to use the CN to assess the singularity of the instrument matrix, we propose a CN based metric to optimize the polarization systems in this paper, as given by

$$\mathbf{b}_o = \arg \min_{b \in \Lambda} \{\kappa_p[\mathbf{D}(\mathbf{b})]\}, \quad (9)$$

where,  $\mathbf{b}$  is a set of systematic parameters including the azimuths and retardance of the polarized elements, which determines the systematic configurations,  $\Lambda$  is the domain for these parameters, and  $\mathbf{b}_o$  stands for the output optimized results for systematic parameters. It can be seen that the optimization process aims to minimize the CN to search for a set of systematic configurations to improve the immunity of the system to the errors.

It should be noted that for a simple polarization system, such as a single-wavelength polarimeter or ellipsometer, we can obtain an ideal configuration by using the proposed optimization metric given by Eq. (9). However, in practice, for a complex polarization system, such as a spectroscopic polarimeter or ellipsometer, the system optimization is usually a compromise process. Anyway, the metric based on the CN given by Eq. (9) provides a basic direction and rule for the optimization of polarization systems. Based on this metric, we can derive specific optimization methods for different systems.

## 3. Superachromatic polarization modulator

The polarization modulator (PM) is the most important part of a polarization system. The polarization modulation completeness and stability and the applicable spectral range of the PM determine key performances of the polarization system. Here, we propose a novel architecture based on a LP combining with a sequence of parallel LRs, as shown in Fig. 2. The LR sequence acts as the rotating compensator (RC) as a whole, which is rotated continuously to achieve complete polarization modulation. Each LR in the sequence is a quarter-wave plate made from birefringent materials, such as the magnesium fluoride and quartz. Compared with conventional designs, the single waveplates in the proposed polarization modulator are not limited to specific structures, and both central wavelengths and axis orientations of the single-waveplates are flexible

parameters, which can provide approximately twice as many degrees of freedom to accommodate the optimization of broadband polarization systems. The proposed architecture has capacity to achieve complete and stable polarization modulation over ultra-wide spectral ranges, and thus is called the superachromatic PM. Based on the general theoretical aspects addressed in Sec. 2, the working principle, optimal design, and in-situ calibration method for the proposed superachromatic PM will be discussed in details in this part.

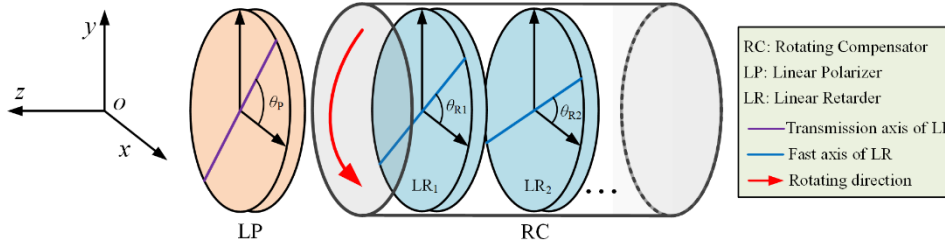


**Fig. 2.** Schematic of the proposed polarization modulator based on a linear polarizer and a sequence of parallel linear retarders.

### 3.1. Working principle

As shown in Fig. 2, in the framework of the proposed PM, the LP and all the LRs are parallel arranged in the  $x$ - $o$ - $y$  plane. Thus, it can be used as a PSA/PSG when the light propagates positive/negative direction along the  $z$ -axis. Based on the proposed PM, we can develop various polarization systems, as schematically shown in Fig. 3. These typically include a rotating-compensator Stokes polarimeter (RCSP), two rotating-compensator ellipsometers (RCE) with different configurations, and a dual rotating-compensator Mueller matrix ellipsometer (DRC-MME) [2,3]. Since the proposed PM can achieve complete polarization modulation, the PSG and PSA based on the proposed PM can generate and analyze polarized light of any polarization state, respectively. As shown in Fig. 3(a), The RCSP contains only one complete PSA and can be applied to detect the full Stokes vector of the polarized light. While the DRC-MME contains both the PSG and the PSA as shown in Fig. 3(d), and therefore can measure the complete  $4 \times 4$  Mueller matrix of the sample. Different from the DRC-MME and the RCSP, the RCE contains one complete PSA or PSG and an additional LP as shown in Fig. 3(b) and 3(c), and can measure only part of the Mueller Matrix (at most a  $4 \times 3$  or  $3 \times 4$  block) [2].

Since we have proved that the PSG is equal to the PSA with the same configurations in the view of polarization matrix optics, for simplicity, here we only take the case of PSA as an example to present the theoretical derivations of the working principle of the proposed PM. First of all, we will check the polarization properties of the sequence of parallel LRs, i.e., the RC, whose Mueller matrix can be calculated by

$$\mathbf{M}_{\text{RC}}(\lambda) = \prod_{m=M}^1 \mathbf{M}_{\text{LR}m}(\lambda) = \prod_{m=M}^1 \mathbf{R}(-\theta_{Rm}) \mathbf{M}(\delta_{Rm}(\lambda)) \mathbf{R}(\theta_{Rm}), \quad (10)$$

where,  $\mathbf{M}_{\text{LR}m}$ ,  $\theta_{Rm}$ , and  $\delta_{Rm}$  ( $m = 1, 2, \dots, M$ ) are the Mueller matrix, azimuth with respect to the  $x$ -axis, and the linear retardance of the  $m$ -th LR in the sequence, respectively. Due to the dispersion in materials, the linear retardance  $\delta_{Rm}$  is usually wavelength-dependet. According to Jones' equivalence theorems [98], the above RC can be optically treated as a combination of a

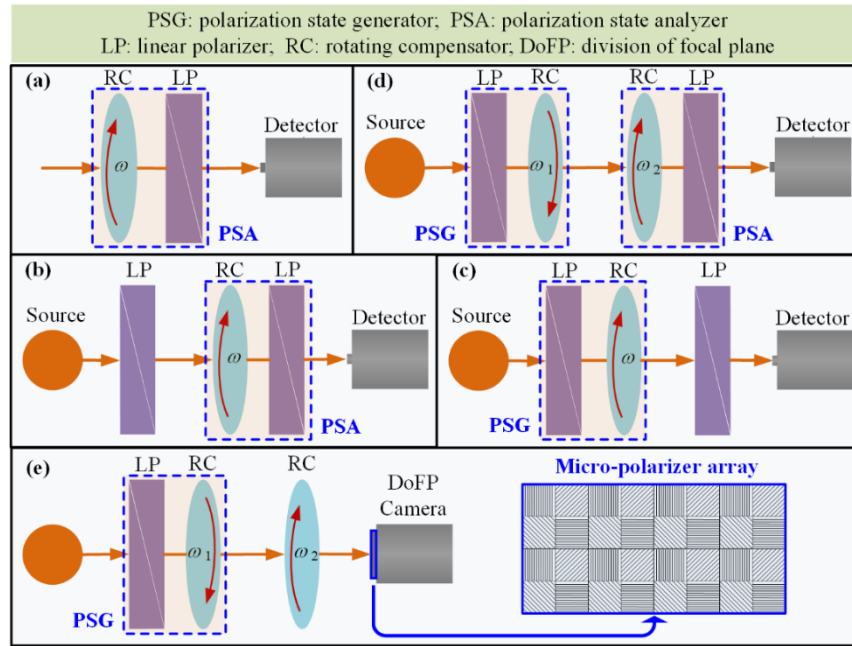


**Fig. 3.** Typical polarization systems based on the proposed polarization modulator: (a) a full Stokes polarimeter; (b) and (c) two configurations of incomplete Mueller matrix ellipsometers based on single rotating compensator; (d) the complete Mueller matrix ellipsometer based on dual rotating compensators; (e) the complete imaging Mueller matrix polarimeter based on the rotating compensator and DoFP polarization camera [71].

LR and an optical rotator (also known as circular retarder). Equation (10) can be rewritten as

$$\mathbf{M}_{\text{RC}}(\lambda) = \mathbf{R}(\rho_e(\lambda))\mathbf{R}(-\theta_e(\lambda))\mathbf{M}(\delta_e(\lambda))\mathbf{R}(\theta_e(\lambda)), \quad (11)$$

where,  $\delta_e$ ,  $\theta_e$  and  $\rho_e$  are the equivalent linear retardance, equivalent fast axis azimuth, and equivalent rotation angle (also known as the circular retardance). These equivalent parameters are wavelength-dependent, and can be totally determined by the structural parameters of the sequence of parallel LRs, including the azimuth  $\theta_{Rm}$  and retardance  $\delta_{Rm}$ . Thus, the system transfer function of the PSA can be written in the following Stokes-Mueller formulism

$$\mathbf{S}_{\text{out}} = \mathbf{M}_{\text{LP}}\mathbf{M}_{\text{RC}}\mathbf{S}_{\text{in}} = [\mathbf{R}(-\theta_p)\mathbf{M}_P\mathbf{R}(\theta_p)][\mathbf{R}(\rho_e)\mathbf{R}(-\theta_e)\mathbf{M}(\delta_e)\mathbf{R}(\theta_e)]\mathbf{S}_{\text{in}}, \quad (12)$$

where,  $\mathbf{S}_{\text{in}}$  and  $\mathbf{S}_{\text{out}}$  are the Stokes vectors entering and exiting the PSA respectively, and  $\theta_p$  is the transmission axis azimuth of the LP with respect to the  $x$ -axis. Since the compensator is rotated continuously, we have  $\theta_e = \omega t - \theta_{e0}$ , where  $\omega$  and  $\theta_{e0}$  are the mechanical angular frequency of the rotation and the original equivalent fast axis azimuth (i.e., at the time  $t=0$ ) of the compensator.

By multiplying the matrices in Eq. (12), the expression for the irradiance at the detector (proportional to the first element of  $\mathbf{S}_{\text{out}}$ ) can be described as the following Fourier series [42]

$$I(t) = a_0 + \sum_{n=1}^2 [\alpha_{2n} \cos(2n\omega t) + \beta_{2n} \sin(2n\omega t)], \quad (13)$$

where,  $a_0$  and  $(\alpha_{2n}, \beta_{2n})$  are the d.c. and d.c.-normalized a.c. Fourier coefficients, which are functions of systematic parameters including  $\theta_p$ ,  $\delta_e$ ,  $\rho_e$  and  $\theta_{e0}$ , and  $n$  ( $n = 1, 2$ ) is the order of

the Fourier coefficient. The Fourier coefficients are linear combinations of the Stokes vector elements  $S_j$  ( $j = 1, 2, 3, 4$ ) in  $\mathbf{S}_{in}$  to be determined. To detect the waveform given in Eq. (13), one can perform  $K$  times integrals of the irradiance over the fundamental optical period of  $\pi/\omega$ , which leads to raw flux data  $\{i_k, k = 1, 2, \dots, K\}$  of the form [44]

$$i_k = \int_{\frac{(k-1)\pi}{K\omega}}^{\frac{k\pi}{K\omega}} I(t) dt = \frac{\pi a_0}{K\omega} + \sum_{n=1}^2 \frac{a_0}{n\omega} \left( \sin \frac{n\pi}{K} \right) \left[ \alpha_{2n} \cos \frac{(2k-1)n\pi}{K} + \beta_{2n} \sin \frac{(2k-1)n\pi}{K} \right]. \quad (14)$$

From Eqs. (13)-(14), we know that the relation between the Stokes vector elements  $S_j$  and the measured fluxes  $i_k$  is essentially a linear transformation. Thus, finally the linear equations of Eq. (14) can be rewritten in the matrix form as given in Eq. (2), with the systematic parameter set  $\mathbf{b} = [\theta_p, \delta_e, \rho_e, \theta_{e0}]$ .

Equations (10)-(14) give the basic working principle for the PSA based on the proposed PM. It can be easily extended to the PSG as well as other polarization systems shown in Fig. 3 by just using the equivalence and reversibility theorems given in Sec. 2.2. It should be noted that, if we want to obtain the full Stokes vector, the integral number should satisfy  $K \geq 4$ . In this case, with a well-conditioned configuration, the instrument matrix rank of the proposed PM satisfies  $r(\mathbf{D}) \geq 4$ , indicating that it can achieve complete polarization modulation.

### 3.2. Optimal design method for an ultra-wide spectral range

The framework of the proposed PM can be totally determined by the systematic parameters  $\mathbf{b} = [\theta_p, \delta_e, \rho_e, \theta_{e0}]$ . It has been proved that the rotation angle is an independent parameter in the RC-based systems and can be incorporated into the azimuths of the LR and the LP [87], and has exactly no effect on the performance of the proposed PM. We can check the influences of these parameters on the polarization modulation performance by calculating the CN of the instrument matrix versus these systematic parameters. Figures 4 and 5 respectively show the CN curves versus the retardance  $\delta_e$  of the equivalent LR, and versus the azimuths  $(\theta_p, \theta_{e0})$  of the LP and the equivalent LR. It can be seen that the retardance has much more significant influence on the CN than the azimuths, which is highly consistent with the conclusion on a dual rotating-retarder Mueller matrix system reported in previous work [39]. As shown in Fig. 4, within the range of  $0 \sim 360^\circ$ , the CN curves versus the retardance are symmetric about  $\delta_e = 180^\circ$ . The CN curves show slightly different when using different norms  $p$ . The minimum CN and the corresponding retardance for different norms are comparatively summarized in Table 1. For an example, the 2-norm CN has the minimum value of 1.863 when the retardance is  $128.6^\circ$  or  $231.4^\circ$ . Compared to the retardance, the azimuths show ignorable contributions to the CN. In fact, if we use the 2-norm, the axis azimuths have exactly no influences on the CN. As shown in Fig. 5, even if we use the  $\infty$ -norm and 1-norm, the deviations in the CN resulted by the azimuths are less than 3% and 6%, respectively. Therefore, in the optimization of the proposed PM, we can spend our efforts mainly focusing on the equivalent retardance of the LR sequence. As shown in Fig. 4 and Table 1, the optimal retardance is about  $128^\circ \sim 133^\circ$  or  $227^\circ \sim 232^\circ$ , which agrees well with the reported optimal values for RC-based polarization systems [73,39,87].

In practice, due to the dispersion in polarization characteristics of the polarized elements, any PM cannot be always performed with the minimum CN over a wide spectral range. As stated above, the proposed framework contains a series of LRs made of birefringent quarter-wave plates, which makes it can be used as a complete PM over a wide spectral range. The retardance of the birefringent quarter-wave plate is wavelength dependent due to the dispersive birefringence of the material, and can be calculated by

$$\delta_{Rm}(\lambda) = \frac{\pi}{2} \frac{\lambda_{Rm}}{\lambda} \frac{\Delta n(\lambda)}{\Delta n(\lambda_{Rm})} \quad (15)$$

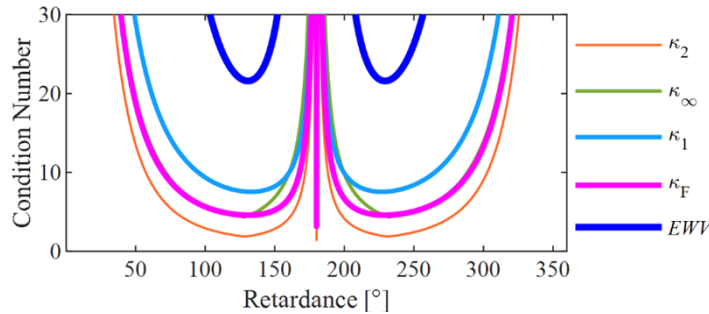


**Fig. 4.** Condition number of the instrument matrix of the proposed polarization modulator versus the retardance of the equivalent linear retarder by using different norms.

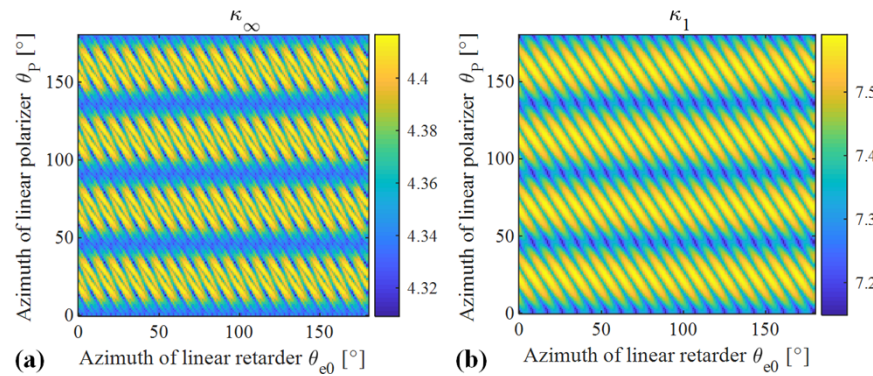


**Fig. 5.** Condition number of the instrument matrix of the proposed polarization modulator versus the azimuths of the equivalent linear retarder and the linear polarizer: (a)  $\infty$ -norm; (b) 1-norm.

**Table 1. Optimal retardance of the rotating compensator under different metrics**

Metrics	Minimum value	Optimal retardance $\delta_e$
$\kappa_2$	1.863	128.6° & 231.4°
$\kappa_\infty$	4.350	128.0° & 232.0°
$\kappa_1$	7.549	132.9° & 227.1°
$\kappa_F$	4.589	130.8° & 229.2°
$EWV$	21.599	130.7° & 229.3°

where, the subscript  $m$  ( $m = 1, 2, \dots, M$ ) refers to index of the quarter-wave plate in the sequence,  $\lambda$  and  $\lambda_{Rm}$  represent the vacuum wavelength and the central wavelength for the  $m$ -th zero-order quarter-wave plate, and  $\Delta n$  is the birefringence of the material. Thus, all the equivalent parameters ( $\delta_e, \theta_e, \rho_e$ ) of the LR sequence (i.e., the RC) can be totally determined by the structural parameters including the central wavelengths  $\lambda_{Rm}$  and the fast axis azimuths  $\theta_{Rm}$  of these zero-order quarter-wave plates. Since the retardances of component LRs in the sequence are dispersive as shown in Eq. (15), all the equivalent parameters ( $\delta_e, \theta_e, \rho_e$ ) are wavelength-dependent. In the design of a such PM, the structure of the framework should be optimized to make it exhibit with a balanced and lowest CN spectrum over the applicable spectral range.

It should be noted that the LR sequence in the proposed framework has a more general structure with the axes of the component LRs arbitrarily arranged, which is different from those specific structures with axes arranged parallel/perpendicular or symmetrically in conventional composite LRs [76,77]. Although the general structure introduces the side effect that the RC is no longer a purely LR but a general elliptical retarder containing both linear retardance and circular retardance (i.e., rotation angle), it provides about twice degrees of freedom for the optimization over wide spectral range than the traditional designs with specific structures. In a polarization system, what we care about is the total effect of the compensator on the CN of the system, but not whether it is a LR or not. Additionally, we have proved that the rotation angle is not an independent parameter in the RC-based systems and can be incorporated into the azimuths of the LR and the LP [87], and has negligible effect on the optimization of the system. Based on these considerations, we can optimize the performance of the proposed PM over an ultra-wide spectral range by using the CN metric as described in Sec. 2.3. Here we define a parameter to evaluate the achromatism of the CN of the PM over a spectral range, as given by

$$Ach_\kappa = \max_{\lambda \in \Gamma} [\kappa(\lambda) - \kappa_{\min}], \quad (16)$$

where,  $Ach_\kappa$  is named as the achromatism of the CN, the  $\kappa(\lambda)$  and  $\kappa_{\min}$  are respectively the CN at the working wavelength  $\lambda$  and the minimum value as given in Fig. 4 and Table 1, and  $\Gamma$  is the domain for the applicable wavelength range of the PM. Compared with the retardance, the most commonly used evaluation criterion for achromatism, the criterion based on the condition number is more suitable to evaluate and optimize the overall performance of the polarization system. The optimization aims to minimize the achromatism of the instrument matrix CN over a wide spectral range as given by

$$(\lambda_o, \theta_o) = \arg \min_{(\lambda, \theta) \in \Lambda} [\tau(\lambda) Ach_\kappa], \quad (17)$$

where,  $(\lambda, \theta) = \{(\lambda_{Rm}, \theta_{Rm}); m = 1, 2, \dots, M\}$  are the central wavelengths and the fast axis azimuths of the component single waveplates, and  $(\lambda_o, \theta_o) = \{(\lambda_{Rmo}, \theta_{Rmo}); m = 1, 2, \dots, M\}$  are the optimal values for the central wavelengths and the fast axis azimuths of the single waveplates,  $\Lambda$  is the domain for the design parameters of the single waveplates, and  $\tau(\lambda)$  is a weighting factor, which is introduced to take into account of the wavelength-dependent signal-to-noise level of the polarization system. Therefore, we can optimize the structure of the proposed PM according to the metric given in Eq. (17) to achieve superachromatic and lowest CN over an ultra-wide spectral range.

### 3.3. In-situ calibration method

In the proposed PM, the systematic parameters  $\mathbf{b} = [\theta_P, \delta_e, \rho_e, \theta_{e0}]$  can be in-situ calibrated in the RC-based polarization systems as shown in Fig. 3. It should be noted that the equivalent rotation angle  $\rho_e$  is not an independent parameter, and it can be incorporated into the axis azimuths  $\theta_P$  and  $\theta_{e0}$ . The relations between the rotation angle and the axis azimuths depend on the specific configuration of the polarization system. For example, in the RCSP as shown in Fig. 3(a), the

rotation angle  $\rho_e$  can be totally incorporated into the axis azimuth of the LP  $\theta_P$ . When the original axis azimuth of the polarizer is set as 0, we have the relation  $\theta_P = \rho_e$ .

Generally, the systematic parameters can be calibrated by solving the Fourier coefficient functions for the RC-based polarimetry system [44,75]. However, the systematic parameters calibrated by this method may contain a lot of noise and systematic errors. To eliminate the influences of these errors on the calibration results, here we propose a wavelength-by-wavelength regression method to calibrate the spectra of the systematic parameters by using a standard sample. In the calibration, the experimental Fourier coefficients are firstly calculated by measuring the irradiance integrals with the standard sample according to Eq. (14). Then, the theoretical Fourier coefficients can be calculated by using the information of the standard sample and the given systematic parameters according to system model shown in Eqs. (12) and (13). At last, the theoretical Fourier coefficients are fitted to the experimental ones by minimizing the  $\chi^2$  error, which is defined as

$$\chi^2 = \sum_n \left\{ \left[ \frac{\alpha_{2n}^e - \alpha_{2n}^t(\mathbf{b})}{\sigma(\alpha_{2n})} \right]^2 + \left[ \frac{\beta_{2n}^e - \beta_{2n}^t(\mathbf{b})}{\sigma(\beta_{2n})} \right]^2 \right\}, \quad (18)$$

where,  $(\alpha_{2n}^e, \beta_{2n}^e)$  and  $(\alpha_{2n}^t, \beta_{2n}^t)$  are the experimental and the theoretical Fourier coefficients respectively, and  $\sigma$  is the standard deviation of the corresponding experimental Fourier coefficient.

As shown in Fig. 6, the fitting procedure is performed by adjusting the systematic parameters  $\mathbf{b}$  with an increment  $\mu$  through an iterative non-linear regression procedure [99]. The regressive iteration continues until that  $\chi^2$  is smaller than the given threshold  $\varepsilon$ . To make the calibration process more efficient, the initial values of the systematic parameters for the first wavelength are given by solving the Fourier coefficient functions, and the output calibrated results are set as the input initial values of the systematic parameters for the next wavelength. In this way, the spectra of the systematic parameters can be *in-situ* calibrated wavelength-by-wavelength.

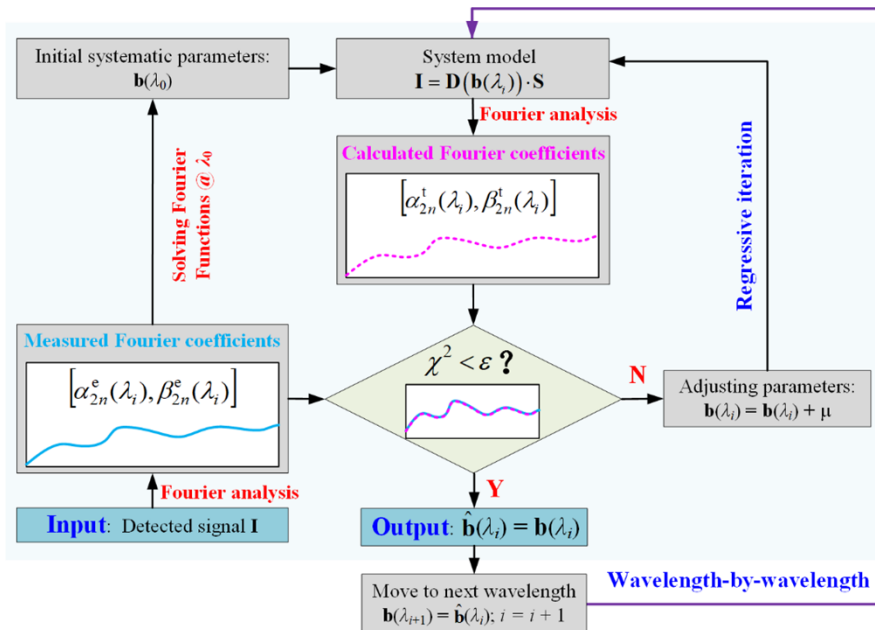


**Fig. 6.** Flowchart of the in-situ calibration of the polarization modulator by a wavelength-by-wavelength regression procedure in the RC-polarimetry system.

#### 4. Results and discussion

In this section, we present the results of the optimal design and *in-situ* calibration of proposed PM used for ultra-broadband polarization systems covering the wavelength range 200~1000 nm. The optimal design process is performed according to the metric shown in Eq. (17), and the 2-norm is utilized to calculate the CN. Since the axis azimuths of the polarized components have ignorable influence on the CN [39], for simplicity, the original orientations of the axes are set parallel to the reference plane of the system (i.e.,  $P_S = 0, \theta_1 = 0$ ) in the optimization of the proposed PM. The *in-situ* calibration procedure is completed on a home-made DRC-MME platform according to the principles as shown in Fig. 6 and Eq. (18). The number of the irradiance integrals over a fundamental optical period is chosen as  $K = 50$ , which will satisfy the Nyquist sampling theorem for all the RC-based polarization systems. The birefringence of the materials involved in this paper can be calculated by Sellmeier's equations [100,101].

In the first case, we assume that the polarization system has a balanced signal-to-noise level over the whole spectral range, thus the weighting factor in Eq. (17) is  $\tau(\lambda) \equiv 1$ . Quartz is chosen as the birefringent material, and the optimal design results are shown in Table 2 and Fig. 7. For convenience, the LR sequence containing  $M$  component single waveplates is called  $M$ -plate in this paper. It can be observed from Table 2 that the  $M$ -plate compensators have general structures, and the central wavelengths and the fast axis azimuths of the single waveplates are optimized values. From Fig. 7, it can be seen the  $M$ -plate compensators are elliptical retarders, containing both the linear retardance and the rotation angle. Although the  $M$ -plate compensators exhibit strong dispersion in the fast axis azimuth and the rotation angle, they have superachromatic retardance around the optimal value 128.6° over the whole spectral range, providing much flat CN spectra close to the minimum value of 1.863 shown in Table 1. The achromatism of the retardance and the CN improves as the number ( $M$ ) of the single-waveplates increases, and the achromatic coefficients  $Ach_K$  of the CN over the entire spectral range are 0.72, 0.14 and 0.09 for the quartz 3-plate, 4-plate and 5-plate, respectively.

**Table 2. Structure parameters for quartz M-plate compensators optimized over spectral range of 200~1000 nm**

$M$	Central wavelengths (nm)					Fast axis azimuths (°)					$Ach_K$
	$\lambda_{R1}$	$\lambda_{R2}$	$\lambda_{R3}$	$\lambda_{R4}$	$\lambda_{R5}$	$\theta_{R1}$	$\theta_{R2}$	$\theta_{R3}$	$\theta_{R4}$	$\theta_{R5}$	
3	792.5	1014.3	705.1	-	-	0	64.8	17.0	-	-	0.72
4	1171.3	489.2	504.0	725.5	-	0	77.0	56.0	19.3	-	0.14
5	753.7	270.4	496.1	740.0	1045.3	0	52.2	20.9	90.0	27.3	0.09

It should be noted that in theory, introducing more plates will produce flatter and smaller condition number spectrum. However, in practice, more plates may significantly increase the manufacturing difficulty especially in the assembly and axis alignment. In this case, not only the cost will significantly increase, but also more manufacturing and installation errors will be introduced to the system. In addition, when the plate number is larger than 4, the performance improvement by increasing the number of plates is limited. Therefore, the choice of plate number is a compromise between the performance and cost. Actually, a 4-plate compensator performs good enough for the RC-based polarization systems covering the UV-VIS-NIR range.

To highlight the advantages of the proposed PM based on the  $M$ -plate, Fig. 8 shows the comparison between CN spectra of the  $M$ -plate and typical conventional composite achromatic waveplates including Beckers waveplate [77], Pancharatnam waveplate [76] and superachromatic waveplate [79]. These composite waveplates are optimized according to a metric similar to Eq. (17) but with the constraint of specific structures of the single waveplates by minimizing the achromatism of the CN over the spectral range of 200~1000 nm. It can be observed from Fig. 8 that the quartz 4-plate has the flattest CN spectrum, which is slightly smaller than the

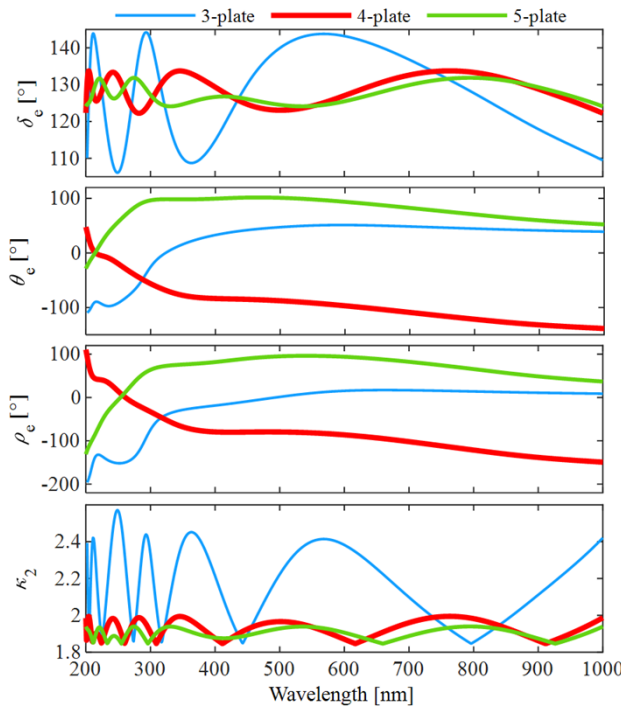


**Fig. 7.** Spectra of the systematic parameters and the condition number of the optimally designed polarization modulator based on a linear polarizer and a sequence of birefringent waveplates.

that of the superachromatic waveplate, and is much smaller and flatter than those of the others. However, the proposed 4-plate also has a much simpler structure than the superachromatic waveplate, since it contains only 4 single waveplates made of the same material, while the superachromatic waveplate contains 6 single waveplates made of two different materials. The Pancharatnam superachromatic waveplate is extremely difficult to fabricate and costly, and much more manufacturing errors especially in the assembly and axis alignment may significantly reduce the actual performance. These results confirm that the general structure of the proposed  $M$ -plate provides more flexibilities to adapt to the optimization of superachromatic PM over an ultra-wide spectral range.

In the second case, we take the wavelength-dependent signal-to-noise level of the polarization system into account in the optimization. In some sense, the CN can be treated as an amplification factor for the errors in the polarization system. Usually, in the UV wavelength range, the detector has poor radiation response and the optical elements have low transmittance and large imperfections, which results in low signal-to-noise level [87]. Thus, the weighting factor  $\tau(\lambda)$  is introduced to balance the wavelength-dependent signal-to-noise level of the polarization system. Figure 9 presents the results of a quartz 4-plate optimized with empirical weighting factors  $\tau(\lambda) = 4$  for 200~350 nm and  $\tau(\lambda) = 1$  for 350~1000 nm. The central wavelengths and the fast axis azimuths of the single waveplates in the quartz 4-plate are (1074.7nm, 433.4nm, 494.6nm, 598.2nm) and ( $0^\circ$ ,  $77.2^\circ$ ,  $51.1^\circ$ ,  $14.1^\circ$ ), respectively. It can be seen from Fig. 9 that the spectra of the retardance and the CN over the spectral range of 200~350 nm are much closer to the optimal values than those over the remainder range. The achromatic coefficients  $Ach_k$  of the CN are 0.07 and 0.28 for 200~350 nm and 350~1000 nm, respectively.

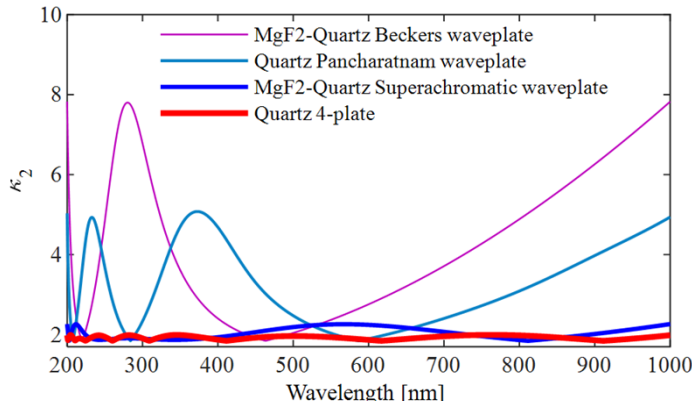


**Fig. 8.** Comparison between the condition spectra of the polarization modulator based on the optimally designed quartz 4-plate and typical conventional composite waveplates including the MgF<sub>2</sub>-quartz Berkers waveplate, the quartz Pancharatnam waveplate and the MgF<sub>2</sub>-quartz superachromatic waveplate.

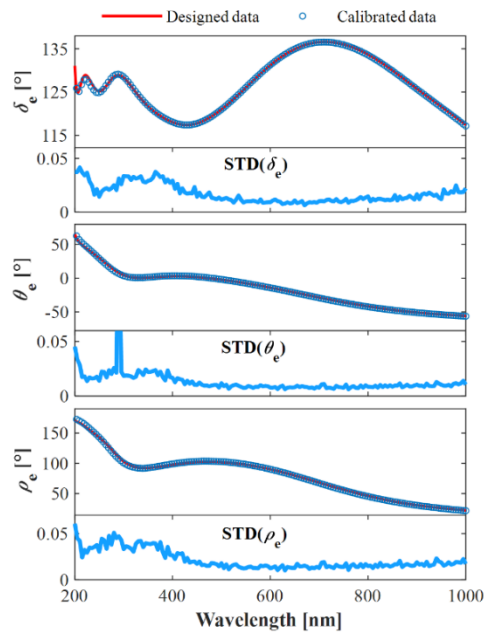


**Fig. 9.** Designed and calibrated results of the proposed polarization modulator based on quartz 4-plate optimized with weighting factors  $\tau = 4$  for 200~350 nm and  $\tau = 1$  for 350~1000 nm. STD represents the standard deviations of the calibrated results under 30 times repeated calibrations.

In the fabrication of the optimized *M*-plate, there are two key process steps, i.e., the fabrication of the zero-order quarter waveplates and the internal axis alignment of the single waveplates [75,102]. Since the thickness of a true zero-order quartz plate is only tens of microns that is too thin to be cut and polished, the common practice is to combine two thick plates with their fast axes aligned perpendicular to each other to make a compound zero-order waveplate. However, the compound zero-order waveplate will suffer from various artifacts due to the misalignment between the axes [75,102,103]. To overcome these practical difficulties, the quartz crystal is cemented on the JGS1 optical glass substrate and then can be polished to true zero-order waveplates. Then the single waveplates are cemented together with their fast axes aligned at the optimally designed orientations. All the plates as well as the substrates directly contact each other without any air gap by using optical cement method, which reduces the interference effects and improves the transmittance of the polarized light. The *M*-plate is protected in cylindrical mount engraved with the fast axis direction of the first single waveplate as the reference of the global orientation. The *M*-plate compensator is fabricated by cemented the single waveplates of the optimized central wavelengths together with the fast axes arranged at the optimal orientations [87,102–105]. Finally, by combining the *M*-plate sequence with a LP, such as a Rochon prism, we can implement the proposed superachromatic PM. The *M*-plate is as a whole rotated by a hollow motor and used as the RC in the PM.

Then the polarization characteristic spectra of the PM based on the optimized *M*-plate compensator are *in-situ* calibrated in the RC-based polarization system by the proposed regressive fitting procedure. In this paper, the calibration process is performed on a home-made DRC-MME platform at the reflective measurement mode with an incident angle of 60° using a SiO<sub>2</sub> film on Si substrate with a nominal thickness of 100 nm as the standard calibration sample. The working principles and instrumentation of the home-made MME have been presented in our previous work [87]. The PM to be calibrated is mounted on the detection arm and used as the PSA of the MME, and the global orientation of the *M*-plate and the transmission axis of the LP (here called the analyzer) are set parallel to the incident plane of the system. Figure 9 shows the calibration results of the proposed PM based on the quartz 4-plate optimized with weighting factor, compared with the designed results. It can be seen that the calibrated results agree very well with the designed results, which demonstrates the effectiveness of the proposed method for the *in-situ* calibration of the PM. Differences especially over the UV spectral range are due to fabrication errors in thicknesses and alignment of single waveplates and the noises and systematic errors of the MME system. The standard deviations (STD) of these calibrated parameters under 30 times repeated calibrations are also given to fully check the performance, as shown in Fig. 9. It can be seen that the standard deviations are less than 0.05° for all the three parameters over almost the whole concerned spectral range, indicating the stable and uniform performances of the PM.

To further check the performances of the fabricated PM, the rank *r* and 2-form CN  $\kappa_2$  of its instrument matrix are calculated by the designed and calibrated parameters, as shown in Fig. 10. It can be observed that the rank remains a constant 4 over the whole spectral range, indicating the proposed PM can completely modulate and detect the polarization state described by the Stokes-Mueller formulism. In addition, the CN keeps an extremely flat curve close to the minimum value 1.863, which indicates the ultra-stable performance of the proposed PM. These results again confirm the complete, stable and uniform performances in polarization modulation of the fabricated PM over an ultra-wide spectral range.

Finally, the performances of a house-made DRC-MME based on the proposed PMs are tested by measuring the Mueller matrix of the air at the straight-through measurement mode. Since the ideal Mueller matrix of the air is a unity matrix, it is a common practice to measure the air to evaluate the performances of an MME. In the experiments, 30 repeated measurements are performed, and the mean values and standard deviations of the results are calculated to

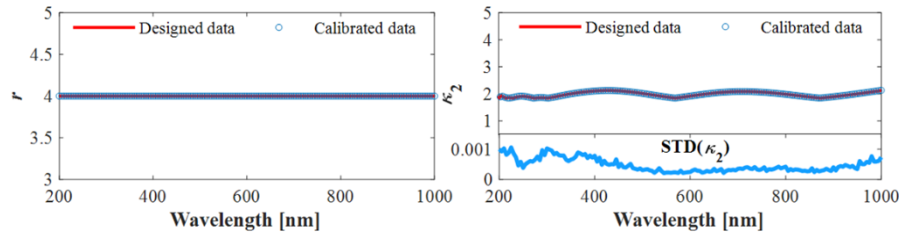


**Fig. 10.** Designed and calibrated rank  $r$  and 2-form condition number  $\kappa_2$  of the instrument matrix of the optimized polarization modulator based on quartz 4-plate.

respectively evaluate the accuracy and precision of the MME. Figure 11 shows the experimental results, and all the Mueller matrix elements ( $M_{ij}$ ,  $i, j = 1, 2, 3, 4$ ) have been normalized by  $M_{11}$ . It can be seen that the biases and standard deviations in all the Mueller matrix elements from their ideal values are respectively less than 0.002 and 0.0006 over the whole spectral range of 200~1000 nm, and additionally they are less than 0.001 and 0.0005 over most of the concerned spectral range. Therefore, the house-made DRC-MME based on the proposed PMs exhibits an accuracy better than 2‰ and a precision better than 0.6‰ for the complete Mueller matrix measurement over the ultra-wide wavelength range of 200~1000 nm, which is the best case for such a broadband MME to the best of our knowledge. Experimental results tested on the DRC-MME further demonstrate the effectiveness and advantage of the proposed PMs for complete, stable and uniform polarization modulation over ultra-wide spectral ranges.

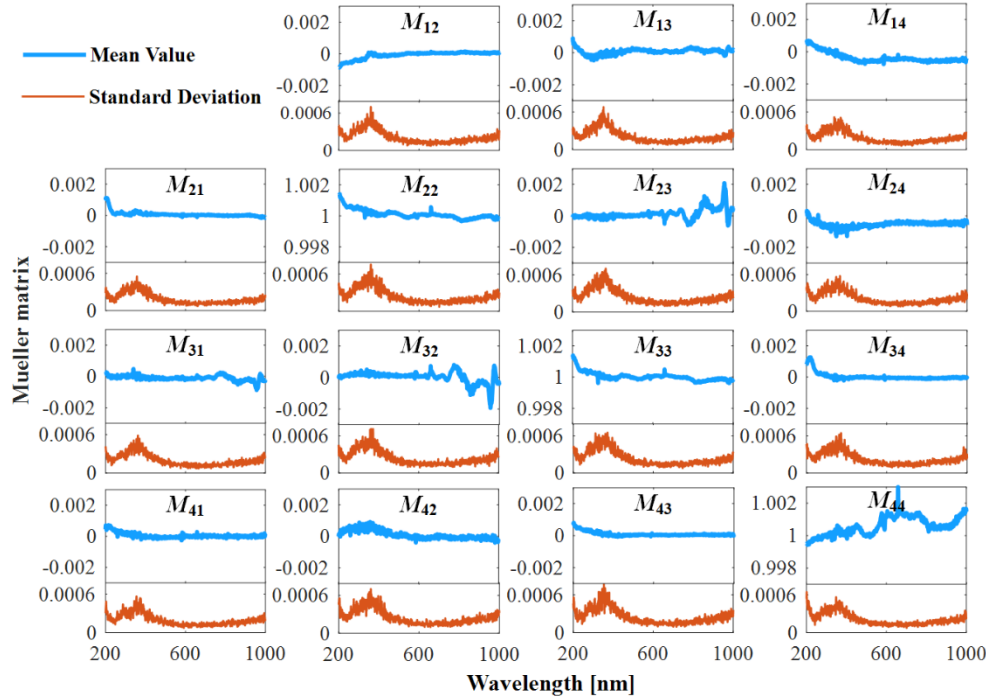


**Fig. 11.** Mean values and standard deviations of the normalized Mueller matrix of 30 repeated straight-through measurements on the air performed on the house-made DRC-MME based on the proposed polarization modulators.

## 5. Conclusions

In summary, we firstly addressed several general theoretical aspects for linear polarization measurement systems by using the matrix algebra, including: (1) a general mathematical model to essentially describe the working mechanism of linear polarization systems; (2) the polarization equivalence theorem for polarized elements and systems based on the reversibility of matrix optics; (3) a general optimization metric for linear polarization systems based on the condition number (CN) of the systematic instrument matrix. Two indices, i.e., the rank and the singularity of the instrument matrix, are defined to respectively evaluate the completeness and stability of the polarization modulation for a linear polarization system. It is pointed out that the polarization state generator (PSG) is mathematically equal to the polarization state analyzer (PSA) with the same configuration. The optimization of a linear polarization system is revealed as to make the instrument matrix as far away from singularity as possible to improve the stability of the system. These theories will provide much convenience and useful guidance for people to well understand, design, calibrate, and operate a linear polarization system.

Based on these theories, we proposed a new framework of superachromatic polarization modulator (PM) consisting of a linear polarizer and a linear retarder (LR) sequence to achieve stable and complete polarization modulation over ultra-wide spectral ranges. Compared to conventional designs, the LR sequence has a general structure and is not limited to specific arrangement to form an achromatic LR, which thereby provides much more flexibility to adapt to broadband polarization modulation. The working principle of the proposed PM is derived based on the Stokes-Mueller formulism and the Jones' equivalent theorem. A new metric based on the CN of the polarization system by considering the wavelength-dependent signal-to-noise is defined to evaluate the achromatism of the PM, and is further utilized to optimize the PM. A wavelength-by-wavelength regression method is proposed to fast and *in-situ* calibrate the PM in a RC-based polarization system over an ultra-wide spectral range.

Finally, several prototypes of the proposed PM were designed and manufactured over the spectral range of 200~1000 nm. Both theoretical and experimental results have demonstrated the validity and great potential of the proposed theories and methods on the optimal design and calibration of the PM. The instrument matrix of the optimized PM keeps a constant rank 4 and an extremely flat condition number close to the minimum 1.863 over the whole concerned spectral range. The fabricated optimized PM is further applied to a home-made dual rotating compensator Mueller matrix ellipsometer, and achieve an accuracy better than 2‰ and a precision better than 0.6‰ for the complete Mueller matrix measurement over the ultra-wide spectral range of 200~1000 nm. These results strongly indicate the capability of the proposed PM for stable, uniform and complete polarization modulation over ultra-wide spectral ranges.

**Funding.** National Natural Science Foundation of China (51727809, 51805193, 52130504); Key Research and Development Plan of Hubei Province (2021BAA013); Natural Science Foundation of Hubei Province (2021CFB322); National Key Research and Development Program of China (2019YFB2005602); National Science and Technology Major Project (2017ZX02101006-004); Fundamental Research Funds for the Central Universities (2021XXJS113).

**Acknowledgments.** The authors thank for the technical support from the Experiment Center for Advanced Manufacturing and Technology in School of Mechanical Science and Engineering (MSE) of HUST. This paper commemorates the 70th anniversary of the MSE of HUST. The authors thank for the continuous support from the MSE of HUST.

**Disclosures.** The authors declare no conflicts of interest.

**Data availability.** Data underlying the results presented in this paper are not publicly available at this time but may be obtained from the authors upon reasonable request.

## References

1. R. M. A. Azzam and N. M. Bashara, *Ellipsometry and Polarized Light*. (Amsterdam, 1977).
2. H. G. Tompkins and E. A. Irene, *Handbook of Ellipsometry*. (Springer, 2005).
3. H. Fujiwara, *Spectroscopic Ellipsometry: Principles and Applications*. (Wiley, 2007).

4. M. Losurdo and K. Hingerl, *Ellipsometry at the Nanoscale*. (Springer, 2013).
5. D. E. Aspnes, "Spectroscopic ellipsometry—past, present, and future," *Thin Solid Films* **571**, 334–344 (2014).
6. S. Liu, X. Chen, and C. Zhang, "Development of a broadband Mueller matrix ellipsometer as a powerful tool for nanostructure metrology," *Thin Solid Films* **584**, 176–185 (2015).
7. R. M. A. Azzam, "Stokes-vector and Mueller-matrix polarimetry [Invited]," *J. Opt. Soc. Am. A* **33**(7), 1396–1408 (2016).
8. J. Hough, "Polarimetry: a powerful diagnostic tool in astronomy," *Astron. Geophys.* **47**(3), 3.31–3.35 (2006).
9. A. Diebold and T. Hofmann, *Optical and Electrical Properties of Nanoscale Materials*. (Springer, 2021).
10. M. Losurdo, "Applications of ellipsometry in nanoscale science: Needs, status, achievements and future challenges," *Thin Solid Films* **519**(9), 2575–2583 (2011).
11. E. Garcia-Caurel, A. De Martino, J. P. Gaston, and L. Yan, "Application of spectroscopic ellipsometry and Mueller ellipsometry to optical characterization," *Appl. Spectrosc.* **67**(1), 1–21 (2013).
12. M. Campoy-Quiles, M. I. Alonso, D. D. C. Bradley, and L. J. Richter, "Advanced ellipsometric characterization of conjugated polymer films," *Adv. Funct. Mater.* **24**(15), 2116–2134 (2014).
13. H. Gu, B. Song, M. Fang, Y. Hong, X. Chen, H. Jiang, W. Ren, and S. Liu, "Layer-dependent dielectric and optical properties of centimeter-scale 2D WSe<sub>2</sub>: evolution from a single layer to few layers," *Nanoscale* **11**(47), 22762–22771 (2019).
14. H. Gu, S. Zhu, B. Song, M. Fang, Z. Guo, X. Chen, C. Zhang, H. Jiang, and S. Liu, "An analytical method to determine the complex refractive index of an ultra-thin film by ellipsometry," *Appl. Surf. Sci.* **507**, 145091 (2020).
15. H. Li, C. Cui, S. Bian, J. Lu, X. Xu, and O. Arteaga, "Model-free determination of the birefringence and dichroism in c-cut crystals from transmission ellipsometry measurements," *Appl. Opt.* **59**(7), 2192–2200 (2020).
16. W. Shen, C. Hu, J. Tao, J. Liu, S. Fan, Y. Wei, C. An, J. Chen, S. Wu, Y. Li, J. Liu, D. Zhang, L. Sun, and X. Hu, "Resolving the optical anisotropy of low-symmetry 2D materials," *Nanoscale* **10**(17), 8329–8337 (2018).
17. S. Funke, M. Duwe, F. Balzer, P. H. Thiesen, K. Hingerl, and M. Schiek, "Determining the dielectric tensor of microtextured organic thin films by imaging Mueller matrix ellipsometry," *J. Phys. Chem. Lett.* **12**(12), 3053–3058 (2021).
18. Z. Guo, H. Gu, M. Fang, B. Song, W. Wang, X. Chen, C. Zhang, H. Jiang, L. Wang, and S. Liu, "Complete dielectric tensor and giant optical anisotropy in quasi-one-dimensional ZrTe<sub>5</sub>," *ACS Mater. Lett.* **3**(5), 525–534 (2021).
19. G. A. Ermolaev, D. V. Grudinin, Y. V. Stebunov, K. V. Voronin, V. G. Kravets, J. Duan, A. B. Mazitov, G. I. Tselyakov, A. Bylinkin, D. I. Yakubovsky, S. M. Novikov, D. G. Baranov, A. Y. Nikitin, I. A. Kruglov, T. Shegai, P. Alonso-Gonzalez, A. N. Grigorenko, A. V. Arsenin, K. S. Novoselov, and V. S. Volkov, "Giant optical anisotropy in transition metal dichalcogenides for next-generation photonics," *Nat. Commun.* **12**(1), 854 (2021).
20. M. Wei, J. Lian, Y. Zhang, C. Wang, Y. Wang, and Z. Xu, "Layer-dependent optical and dielectric properties of centimeter-scale PdSe<sub>2</sub> films grown by chemical vapor deposition," *npj 2D Mater. Appl.* **6**(1), 1–8 (2022).
21. K. Meng, B. Jiang, and K. Youcef-Toumi, "Neural network assisted multi-parameter global sensitivity analysis for nanostructure scatterometry," *Appl. Surf. Sci.* **570**, 151219 (2021).
22. N. G. Orji, M. Badaroglu, B. M. Barnes, C. Beitia, B. D. Bundy, U. Celano, R. J. Kline, M. Neisser, Y. Obeng, and A. E. Vladar, "Metrology for the next generation of semiconductor devices," *Nat. Electron.* **1**(10), 532–547 (2018).
23. S. Liu, W. Du, X. Chen, H. Jiang, and C. Zhang, "Mueller matrix imaging ellipsometry for nanostructure metrology," *Opt. Express* **23**(13), 17316–17329 (2015).
24. Y. Tan, C. Chen, X. Chen, W. Du, H. Gu, and S. Liu, "Development of a tomographic Mueller-matrix scatterometer for nanostructure metrology," *Rev. Sci. Instrum.* **89**(7), 073702 (2018).
25. A. Diebold, A. Antonelli, and N. Keller, "Perspective: Optical measurement of feature dimensions and shapes by scatterometry," *APL Mater.* **6**(5), 058201 (2018).
26. J. S. Tyo, D. L. Goldstein, D. B. Chenault, and J. A. Shaw, "Review of passive imaging polarimetry for remote sensing applications," *Appl. Opt.* **45**(22), 5453–5469 (2006).
27. L. Yan, Y. Li, V. Chandrasekar, H. Mortimer, J. Peltoniemi, and Y. Lin, "General review of optical polarization remote sensing," *International Journal of Remote Sensing* **41**(13), 4853–4864 (2020).
28. L. Yan, B. Yang, F. Zhang, Y. Xiang, and W. Chen, *Polarization Remote Sensing Physics*. (Springer, 2020).
29. T. D. Oswalt and H. E. Bond, *Planets, Stars and Stellar Systems: Volume 2: Astronomical Techniques, Software, and Data*. (Springer, 2013).
30. R. Mignani, A. Shearer, A. Slowikowska, and S. Zane, *Astronomical Polarisation from the Infrared to Gamma Rays*. (Springer, 2019).
31. N. Ghosh and I. A. Vitkin, "Tissue polarimetry: concepts, challenges, applications, and outlook," *J. Biomed. Opt.* **16**(11), 110801 (2011).
32. C. He, H. He, J. Chang, B. Chen, H. Ma, and M. J. Booth, "Polarisation optics for biomedical and clinical applications: a review," *Light: Sci. Appl.* **10**(1), 194 (2021).
33. M. Schubert, "Another century of ellipsometry," *Ann. Phys.* **15**(7-8), 480–497 (2006).
34. R. M. A. Azzam, "The intertwined history of polarimetry and ellipsometry," *Thin Solid Films* **519**(9), 2584–2588 (2011).
35. U. Rossow, "A brief history of ellipsometry," *Phys. Status Solidi B* **256**(2), 1800307 (2019).
36. P. S. Hauge, "Mueller matrix ellipsometry with imperfect compensators," *J. Opt. Soc. Am.* **68**(11), 1519–1528 (1978).

37. R. Kleim, L. Kuntzler, and A. E. Ghemmaz, "Systematic errors in rotating-compensator ellipsometry," *J. Opt. Soc. Am. A* **11**(9), 2550–2559 (1994).
38. L. Broch, A. E. Naciri, and L. Johann, "Systematic errors for a Mueller matrix dual rotating compensator ellipsometer," *Opt. Express* **16**(12), 8814–8824 (2008).
39. M. H. Smith, "Optimization of a dual-rotating-retarder Mueller matrix polarimeter," *Appl. Opt.* **41**(13), 2488–2493 (2002).
40. H. Dai and C. Yan, "Measurement errors resulted from misalignment errors of the retarder in a rotating-retarder complete Stokes polarimeter," *Opt. Express* **22**(10), 11869–11883 (2014).
41. R. M. A. Azzam, "A simple Fourier photopolarimeter with rotating polarizer and analyzer for measuring Jones and Mueller matrices," *Opt. Commun.* **25**(2), 137–140 (1978).
42. R. M. A. Azzam, "Photopolarimetric measurement of the Mueller matrix by Fourier analysis of a single detected signal," *Opt. Lett.* **2**(6), 148–150 (1978).
43. M. Gilliot and A. E. Naciri, "Theory of dual-rotating polarizer and analyzer ellipsometer," *Thin Solid Films* **540**, 46–52 (2013).
44. R. W. Collins and J. Koh, "Dual rotating-compensator multichannel ellipsometer: instrument design for real-time Mueller matrix spectroscopy of surfaces and films," *J. Opt. Soc. Am. A* **16**(8), 1997–2006 (1999).
45. K. Meng, B. Jiang, C. D. Samolis, M. Alrashed, and K. Youcef-Toumi, "Unevenly spaced continuous measurement approach for dual rotating-retarder Mueller matrix ellipsometry," *Opt. Express* **27**(10), 14736–14753 (2019).
46. P. A. Williams, "Rotating-wave-plate Stokes polarimeter for differential group delay measurements of polarization-mode dispersion," *Appl. Opt.* **38**(31), 6508–6515 (1999).
47. S. S. Ivanov, A. A. Rangelov, N. V. Vitanov, T. Peters, and T. Halfmann, "Highly efficient broadband conversion of light polarization by composite retarders," *J. Opt. Soc. Am. A* **29**(3), 265–269 (2012).
48. T. Mu, C. Zhang, Q. Li, and R. Liang, "Achromatization of waveplate for broadband polarimetric system," *Opt. Lett.* **40**(11), 2485–2488 (2015).
49. T. D. Kang, E. Standard, G. L. Carr, T. Zhou, M. Kotelyanskii, and A. A. Sirenko, "Rotatable broadband retarders for far-infrared spectroscopic ellipsometry," *Thin Solid Films* **519**(9), 2698–2702 (2011).
50. E. Garcia-Caurel, A. Lizana, G. Ndong, B. Al-Bugami, C. Bernon, E. Al-Qahtani, F. Rengnez, and A. De Martino, "Mid-infrared Mueller ellipsometer with pseudo-achromatic optical elements," *Appl. Opt.* **54**(10), 2776–2785 (2015).
51. J. M. Bueno, "Polarimetry using liquid-crystal variable retarders: theory and calibration," *J. Opt. A: Pure Appl. Opt.* **2**(3), 216–222 (2000).
52. A. De Martino, Y. K. Kim, E. Garcia-Caurel, B. Laude, and B. Drevillon, "Optimized Mueller polarimeter with liquid crystals," *Opt. Lett.* **28**(8), 616–618 (2003).
53. A. Peinado, A. Lizana, J. Vidal, C. Iemmi, and J. Campos, "Optimization and performance criteria of a Stokes polarimeter based on two variable retarders," *Opt. Express* **18**(10), 9815–9830 (2010).
54. L. M. S. Aas, P. G. Ellingsen, B. E. Fladmark, P. A. Letnes, and M. Kildemo, "Overdetermined broadband spectroscopic Mueller matrix polarimeter designed by genetic algorithms," *Opt. Express* **21**(7), 8753–8762 (2013).
55. L. M. S. Aas, D. G. Skare, P. G. Ellingsen, P. A. Letnes, and M. Kildemo, "Design, optimization and realization of a ferroelectric liquid crystal based Mueller matrix ellipsometer using a genetic algorithm," *Thin Solid Films* **571**, 522–526 (2014).
56. G. E. Jellison Jr and F. A. Modine, "Two-modulator generalized ellipsometry: theory," *Appl. Opt.* **36**(31), 8190–8198 (1997).
57. O. Arteaga, J. Freudenthal, B. Wang, and B. Kahr, "Mueller matrix polarimetry with four photoelastic modulators: theory and calibration," *Appl. Opt.* **51**(28), 6805–6817 (2012).
58. A. Ruder, B. Wright, D. Peev, R. Feder, U. Kilic, M. Hilfiker, E. Schubert, C. M. Herzinger, and M. Schubert, "Mueller matrix ellipsometer using dual continuously rotating anisotropic mirrors," *Opt. Lett.* **45**(13), 3541–3544 (2020).
59. A. Ruder, B. Wright, R. Feder, U. Kilic, M. Hilfiker, E. Schubert, C. M. Herzinger, and M. Schubert, "Mueller matrix imaging microscope using dual continuously rotating anisotropic mirrors," *Opt. Express* **29**(18), 28704–28724 (2021).
60. T. Minamikawa, Y. D. Hsieh, K. Shibuya, E. Hase, Y. Kaneoka, S. Okubo, H. Inaba, Y. Mizutani, H. Yamamoto, T. Iwata, and T. Yasui, "Dual-comb spectroscopic ellipsometry," *Nat. Commun.* **8**(1), 610 (2017).
61. R. Zhang, Y. Gong, M. W. Day, D. Sun, and S. T. Cundiff, "Radio frequency polarization modulation based on an optical frequency comb," *Rev. Sci. Instrum.* **91**(8), 083111 (2020).
62. J. P. B. Mueller, K. Leosson, and F. Capasso, "Ultracompact metasurface in-line polarimeter," *Optica* **3**(1), 42–47 (2016).
63. A. Martinez, "Polarimetry enabled by nanophotonics," *Science* **362**(6416), 750–751 (2018).
64. N. A. Rubin, G. D'Aversa, P. Chevalier, Z. Shi, W. T. Chen, and F. Capasso, "Matrix Fourier optics enables a compact full-Stokes polarization camera," *Science* **365**(6448), eaax1839 (2019).
65. J. Ma, C. Fang, L. Liang, H. Wang, and D. Li, "Full-Stokes polarimeter based on chiral perovskites with chirality and large optical anisotropy," *Small* **17**(47), 2103855 (2021).
66. R. M. A. Azzam, "Division-of-amplitude photopolarimeter (DOAP) for the simultaneous measurement of all four Stokes parameters of light," *Opt. Acta* **29**(5), 685–689 (1982).

67. Y. Cui and R. M. A. Azzam, "Sixteen-beam grating-based division-of-amplitude photopolarimeter," *Opt. Lett.* **21**(1), 89–91 (1996).
68. S. Zhang, H. Jiang, H. Gu, X. Chen, and S. Liu, "High-speed Mueller matrix ellipsometer with microsecond temporal resolution," *Opt. Express* **28**(8), 10873–10887 (2020).
69. J. del Hoyo, L. M. Sanchez-Brea, and J. A. Gómez-Pedrero, "High precision calibration method for a four-axis Mueller matrix polarimeter," *Optics and Lasers in Engineering* **132**, 106112 (2020).
70. X. Li, F. Goudail, P. Qi, T. Liu, and H. Hu, "Integration time optimization and starting angle autocalibration of full Stokes imagers based on a rotating retarder," *Opt. Express* **29**(6), 9494–9512 (2021).
71. X. Li, F. Goudail, and S. C. Chen, "Self-calibration for Mueller polarimeters based on DoFP polarization imagers," *Opt. Lett.* **47**(6), 1415–1418 (2022).
72. J. Ladstein, M. Kildemo, G. K. Svendsen, I. S. Nerbø, and F. Staboe-Eeg, "Characterisation of liquid crystals for broadband optimal design of Mueller matrix ellipsometers," *Proc. SPIE* **6587**, 65870D (2007).
73. F. Staboe-Eeg, M. Kildemo, E. García-Caurel, and M. Lindgren, "Design and characterization of achromatic 132° retarders in CaF<sub>2</sub> and fused silica," *J. Mod. Opt.* **55**(14), 2203–2214 (2008).
74. B. D. Johs, S. E. Green, C. M. Herzinger, D. E. Meyer, and M. M. Liphardt, "Method of constructing a deviation angle self compensating substantially achromatic retarder to compensate beam translation," U. S. Patent 10, 7907280 (2011).
75. J. Lee, P. I. Rovira, I. An, and R. W. Collins, "Alignment and calibration of the MgF<sub>2</sub> biplate compensator for applications in rotating-compensator multichannel ellipsometry," *J. Opt. Soc. Am. A* **18**(8), 1980–1985 (2001).
76. S. Pancharatnam, "Achromatic combinations of birefringent plates. Part II. An achromatic quarter-wave plate," *Proc. - Indian Acad. Sci., Sect. A* **41**(4), 137–144 (1955).
77. J. M. Bechers, "Achromatic linear retarders," *Appl. Opt.* **10**(4), 973–975 (1971).
78. P. Hariharan, "Achromatic and apochromatic halfwave and quarterwave retarders," *Opt. Eng.* **35**(11), 3335–3337 (1996).
79. P. Hariharan and P. E. Ciddor, "Broad-band superachromatic retarders and circular polarizers for the UV, visible and near infrared," *J. Mod. Opt.* **51**(15), 2315–2322 (2004).
80. J. Liu, Y. Cai, H. Chen, X. Zeng, D. Zou, and S. Xu, "Design for the optical retardation in broadband zero-order half-wave plates," *Opt. Express* **19**(9), 8557–8564 (2011).
81. J. L. Vilas, L. M. Sanchez-Brea, and E. Bernabeu, "Optimal achromatic wave retarders using two birefringent wave plates," *Appl. Opt.* **52**(9), 1892–1896 (2013).
82. J. M. Herrera-Fernandez, J. L. Vilas, L. M. Sanchez-Brea, and E. Bernabeu, "Design of superachromatic quarter-wave retarders in a broad spectral range," *Appl. Opt.* **54**(33), 9758–9762 (2015).
83. E. Dimova, W. Huang, G. Popkirov, A. Rangelov, and E. Kyoseva, "Broadband ultra-broadband modular half-waveplates," *Opt. Commun.* **366**, 382–385 (2016).
84. J. L. Vilas and A. Lazarova-Lazarova, "A simple analytical method to obtain achromatic waveplate retarders," *J. Opt.* **19**(4), 045701 (2017).
85. A. Messaadi, M. M. Sanchez-Lopez, A. Vargas, P. Garcia-Martinez, and I. Moreno, "Achromatic linear retarder with tunable retardance," *Opt. Lett.* **43**(14), 3277–3280 (2018).
86. M. Ou, Y. Liu, J. Tang, R. Deng, P. Guo, and L. Lan, "Composite achromatic quartz wave plate with adjustable retardation and temperature insensitivity," *Appl. Opt.* **60**(22), 6665–6670 (2021).
87. H. Gu, X. Chen, H. Jiang, C. Zhang, and S. Liu, "Optimal broadband Mueller matrix ellipsometer using multi-waveplates with flexibly oriented axes," *J. Opt.* **18**(2), 025702 (2016).
88. D. Gottlieb and O. Arteaga, "Optimal elliptical retarder in rotating compensator imaging polarimetry," *Opt. Lett.* **46**(13), 3139–3142 (2021).
89. S. Savenkov, R. Muttiah, E. Oberemok, and A. Klimov, "Incomplete active polarimetry: Measurement of the block-diagonal scattering matrix," *J. Quant. Spectrosc. Radiat. Transfer* **112**(11), 1796–1802 (2011).
90. D. S. Sabatke, A. M. Locke, M. R. Descour, W. C. Sweatt, J. P. Garcia, E. L. Dereniak, S. A. Kemme, and G. S. Phipps, "Figures of merit for complete Stokes polarimeter optimization," *Proc. SPIE* **4133**, 75–81 (2000).
91. D. S. Sabatke, M. R. Descour, E. L. Dereniak, W. C. Sweatt, S. A. Kemme, and G. S. Phipps, "Optimization of retardance for a complete Stokes polarimeter," *Opt. Lett.* **25**(11), 802–804 (2000).
92. K. M. Twietmeyer and R. A. Chipman, "Optimization of Mueller matrix polarimeters in the presence of error sources," *Opt. Express* **16**(15), 11589–11603 (2008).
93. D. Layden, M. F. G. Wood, and I. A. Vitkin, "Optimum selection of input polarization states in determining the sample Mueller matrix: a dual photoelastic polarimeter approach," *Opt. Express* **20**(18), 20466–20481 (2012).
94. M. R. Foreman, A. Favaro, and A. Aiello, "Optimal frames for polarization state reconstruction," *Phys. Rev. Lett.* **115**(26), 263901 (2015).
95. M. R. Foreman and F. Goudail, "On the equivalence of optimization metrics in Stokes polarimetry," *Opt. Eng.* **58**(08), 1 (2019).
96. N. Vansteenkiste, P. Vignolo, and A. Aspect, "Optical reversibility theorems for polarization: application to remote control of polarization," *J. Opt. Soc. Am. A* **10**(10), 2240–2245 (1993).
97. X. Chen, S. Liu, H. Gu, and C. Zhang, "Formulation of error propagation and estimation in grating reconstruction by a dual-rotating compensator Mueller matrix polarimeter," *Thin Solid Films* **571**, 653–659 (2014).

98. H. Hurwitz Jr and R. C. Jones, "A new calculus for the treatment of optical systems. Part II. Proof of three general equivalence theorems," *J. Opt. Soc. Am.* **31**(7), 493–499 (1941).
99. B. Johs, "Regression calibration method for rotating element ellipsometers," *Thin Solid Films* **234**(1-2), 395–398 (1993).
100. S. Chandrasekhar, "The dispersion and thermo-optic behaviour of vitreous silica," *Proc. - Indian Acad. Sci., Sect. A* **34**(4), 275–282 (1951).
101. M. J. Dodge, "Refractive properties of magnesium fluoride," *Appl. Opt.* **23**(12), 1980–1985 (1984).
102. H. Gu, X. Chen, H. Jiang, C. Zhang, W. Li, and S. Liu, "Accurate alignment of optical axes of a biplate using a spectroscopic Mueller matrix ellipsometer," *Appl. Opt.* **55**(15), 3935–3941 (2016).
103. H. Gu, S. Liu, X. Chen, and C. Zhang, "Calibration of misalignment errors in composite waveplates using Mueller matrix ellipsometry," *Appl. Opt.* **54**(4), 684–693 (2015).
104. H. Gu, X. Chen, C. Zhang, H. Jiang, and S. Liu, "Study of the retardance of a birefringent waveplate at tilt incidence by Mueller matrix ellipsometer," *J. Opt.* **20**(1), 015401 (2018).
105. H. Gu, X. Chen, Y. Shi, H. Jiang, C. Zhang, P. Gong, and S. Liu, "Comprehensive characterization of a general composite waveplate by spectroscopic Mueller matrix polarimetry," *Opt. Express* **26**(19), 25408–25425 (2018).